Modeling LoRa Communications in Estuaries for IoT Environmental Monitoring Systems

Miguel Gutiérrez Gaitán, *Member, IEEE*, Pedro M. d'Orey, José Cecílio, Marta Rodrigues, Pedro M. Santos, Luís Pinto, Anabela Oliveira, António Casimiro, *Member, IEEE*, and Luís Almeida, *Senior Member, IEEE*

***Abstract*—Low-power wide-area networks (LPWANs) are extending beyond the conventional terrestrial domain. Coastal zones, rivers, and wetlands, among others, are nowadays common deployment settings for Internet-of-Things nodes where communication technologies such as Long Range (LoRa) are becoming popular. In this article, we investigate large-scale fading dynamics of LoRa line-of-sight (LoS) links deployed over an estuary with characteristic intertidal zones, considering both *shore-to-shore* (S2S) and *shore-to-vessel* (S2V) communications. We propose a novel methodology for path-loss prediction which captures: 1) spatial; 2) temporal; and 3) physical features of the RF signal interaction with the environmental dynamics, integrating those features into the two-ray propagation model. To this purpose, we resort to precise hydrodynamic modeling of the estuary, including the specific terrain profile (*bathymetry*) at the reflection point. These aspects are key to accounting for a reflecting surface of varying altitude and permittivity as a function of the tide. Experimental measurements using LoRa devices operating in the 868-MHz band show major trends in the received signal power in agreement with the methodology's predictions.**

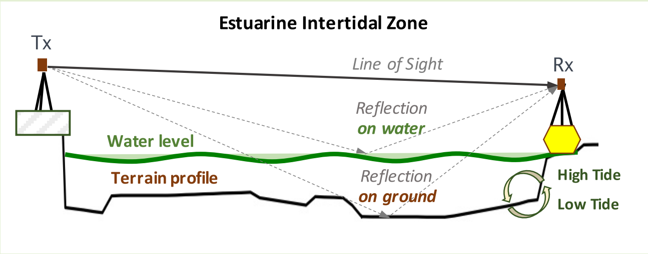

***Index Terms*—Intertidal zone, Long Range (LoRa), overwater communications, path loss, radio-frequency (RF) propagation, tidal fading, two-ray model.**

I. INTRODUCTION

THE protection of water environments is an important challenge for present and future societies around the world. Due to the relevance and timeliness of this issue, the United Nations (UNs) 2030 agenda for sustainable development advocates for access to safe water for all and the sustainable management of water resources in all its aspects [1]. Coastal zones, rivers, estuaries, and wetlands, among others, are examples of fragile ecosystems that are under threat due to pollution (e.g., microplastics), illegal dumping, industrial activities, and water misuse, among many others. These threats can also have devastating consequences for the surrounding wildlife and local populations that make use of available water resources.

To properly protect these aquatic ecosystems, resilient systems should be deployed in selected locations for real-time monitoring of key indicators (e.g., water quality). Nowadays, this task is effectively carried out by static (e.g., [2]) and/or mobile (e.g., [3]) Internet-of-Things (IoT) devices. In particular, low-power wide-area networks (LPWANs), such as Long Range (LoRa), are among the most popular communication protocols enabling low-cost, low-power, and long-range IoT-based monitoring applications [4]. While mostly deployed in terrestrial domains (e.g., urban or rural areas), its applicability in different types of marine and freshwater environments has been demonstrated successfully [5], [6], [7], [8], [9].

Nevertheless, the large-scale adoption of monitoring applications in aquatic scenarios is yet far from being substantial. A major influencing factor is that wireless *over water* communications is affected by multiple environmental issues.

Manuscript received 10 August 2022; accepted 29 August 2022. Date of publication 16 September 2022; date of current version 31 October 2022. This work was supported in part by the National Funds through FCT/MCTES (Portuguese Foundation for Science and Technology), within the CISTER Research Unit under Grant UIDB/04234/2020, the LASIGE Research Unit under Grant UIDB/00408/2020, and the AQUAMON Project under Grant PTDC/CCI-COM/30142/2017; and in part by FCT and by the European Social Fund (ESF) through the Regional Operational Program (ROP) Norte 2020 under Ph.D. Grant 2020.06685.BD. The associate editor coordinating the review of this article and approving it for publication was Prof. Huang Chen Lee. *(Corresponding authors: Miguel Gutiérrez Gaitán; Pedro M. d'Orey.)*

Miguel Gutiérrez Gaitán is with the CISTER Research Center, 4200-135 Porto, Portugal, also with the Faculty of Engineering/Sciences, University of Porto, 4200-465 Porto, Portugal, and also with the Faculty of Engineering, Andrés Bello University, Santiago 8370146, Chile (e-mail: mjggt@isep.ipp.pt).

Pedro M. d'Orey and Luís Almeida are with the CISTER Research Center, 4200-135 Porto, Portugal, and also with the Faculty of Engineering/Sciences, University of Porto, 4200-465 Porto, Portugal (e-mail: ore@isep.ipp.pt; lda@fe.up.pt).

José Cecílio and António Casimiro are with LASIGE, Faculdade de Ciências, Universidade de Lisboa, 1749-016 Lisbon, Portugal (e-mail: jmcecilio@ciencias.ulisboa.pt; casim@ciencias.ulisboa.pt).

Marta Rodrigues and Anabela Oliveira are with LNEC, 1700-075 Lisbon, Portugal (e-mail: mfrodrigues@lnec.pt; aoliveira@lnec.pt).

Pedro M. Santos is with the CISTER Research Center, 4200-135 Porto, Portugal (e-mail: pss@isep.ipp.pt).

Luís Pinto is with the Faculdade de Ciências, Universidade de Lisboa, 1749-016 Lisbon, Portugal (e-mail: lmpinto@fc.ul.pt).

Digital Object Identifier 10.1109/JSEN.2022.3205760

Specifically, distinctive conditions such as tides or waves still require further characterization and modeling. Although it is well established that these phenomena may impair the link quality (e.g., [10], [11], [12], [13], [14], and [15]), specific circumstances such as the recurrent flooding and drying of the so-called *intertidal zones*[1] [16] are generally ignored from a radio propagation perspective. This gap has yet to be addressed for LoRa communication devices operating in the 868-MHz radio-frequency (RF) band, communication technology that we use for validation purposes.

In this work, we focus on the theoretical modeling and experimental validation of the large-scale fading dynamics of line-of-sight (LOS) RF links deployed over estuaries, specifically considering the impact of the intertidal zones. To this purpose, we propose a novel methodology for path-loss prediction that captures: 1) *spatial*; 2) *temporal*; and 3) *physical features* of the RF signal interaction with the (estuarine) tidal dynamics, integrating those features into the well-known two-ray propagation model [17]. The key idea is to obtain the parametric inputs for the two-ray model (e.g., antenna heights) based on the tide-driven shifting of the reflection point, that is, the point that determines both the relative height of the antennas to the surface medium and its relative permittivity (e.g., water or soil with varying water content). To accomplish this with high precision, we resort to state-of-the-art hydrodynamic modeling of an estuary [18], [19], which provides water-level estimations at any point along the link path (*spatial*) and the tidal cycle (*temporal*), but also the corresponding water content of the soil (*physical*) of the reflection point. This latter aspect is crucial for the path-loss estimation in the estuarine intertidal zone, since if the reflection point falls within this area, it will vary from dry to wet regions (or vice versa) following the tide dynamics, also possibly changing the relative altitude with respect to the antennas due to specific terrain profile (bathymetry).

The proposed methodology is evaluated using data from two experimental campaigns conducted at the bay of Seixal, Tagus Estuary, Portugal. These campaigns target both *shore-to-shore* (S2S) and *shore-to-vessel* (S2V) links, for which the time-varying reflection point falls within the intertidal zone. The latter case considers that one of the nodes is installed on a floating platform (e.g., as in the case of a moored boat), which floats only during part of the tidal cycle and sits on the mud during the low tide. As for the hydrodynamic model, we resort to state-of-the-art methods—calibrated using empirical data for Tagus estuarine region—to obtain precise water-level measurements at the space- and time-evolving reflection point.

To the best of our knowledge, the methodology herein proposed pioneers in modeling large-scale fading of (LoRa) links in estuaries, both from the perspective of channel modeling over the intertidal zone as well as from the viewpoint of incorporating precise and location-dependent hydrodynamic features to aid (deterministic) path-loss estimation. Note that, without loss of generality, the methodology is applicable to different tidal environments and corresponding intertidal zones (e.g., at the marine shoreline) for which both location-specific bathymetry and tidal data are commonly available. The main contributions of this work can be summarized as follows.

1) An insightful investigation of the impact of tides in LoRa communication over estuarine waters with intertidal zones.
2) A novel methodology for path-loss prediction in tidal environments based on the nontrivial integration of the two-ray model and a precise hydrodynamic model with location-specific data.
3) A validation of the proposed methodology with real-world measurements for both S2S and S2V link scenarios.

The remainder of the article is organized as follows. The relevant related work is presented in Section II. The novel methodology to model the large-scale fading of RF links operating over estuarine waters is given in Section III. The hydrodynamic model for determining tidal dynamics with the improved temporal and spatial resolution is described in Section IV. The two-ray channel model both for S2S and S2V communication links is revisited in Section V. The experimental measurement campaigns at the Tagus Estuary are detailed in Section VI. The empirical results and the validation of the proposed methodology are reported and discussed in Section VII. Concluding remarks and future work directions are given in Section VIII.

II. RELATED WORK

The relevant state-of-the-art works have been classified into three categories: 1) tidal fading; 2) intertidal zones; and 3) RF propagation over mixed/water land paths. While the literature on RF propagation for maritime communication is much broader (see the review papers in [20] and [21]), we restricted the interest of this section to those works matching more closely the distinguishing aspects of our research, that is, the impact of tides and the intertidal zone in RF signal propagation. Likewise, despite not considering literature beyond the maritime domain, we recognize the existence of further research proposing related procedures or methodologies for LoRa-based sensing systems in specific environments (e.g., mountains [22]) that exploit local conditions for improved path-loss estimation.

A. Tidal Fading

Wireless RF propagation in water environments is known to be affected by multiple factors [20], [21] including the natural oscillations of the water surface. Specifically, tides and waves are among the most common phenomena heavily affecting RF propagation due to the changes in the water level. Prior literature that has recognized and addressed this situation (e.g., [8], [10], [11], [12], [13], [14], [15]) still shows several gaps from the perspective of channel modeling and characterization.

Tides, particularly, can lead to a severe but barely explored condition known as *tidal fading* [10], that is, path-loss changes

---

[1] Intertidal zones correspond to areas that are repeatedly covered and uncovered by water as the tide rises and falls, respectively.

induced by the varying (relative) antenna heights of the nodes with respect to the surface resulting from the recurrent influence of floods and ebbs. Despite some aspects of this phenomenon having been effectively described by the two-ray model (e.g., [23], [24], [25], [26], [27]), further investigations on diverse environmental settings (e.g., estuaries and wetlands), using emerging communication technologies (e.g., LoRa) and/or incorporating precise tidal modeling methods, are still scarce.

Traditionally, research reporting and/or mitigating tidal fading have typically focused on kilometric RF links [10], [11], [13], [23], [24], [28], often using antennas installed at several meters above surface. This is in contrast with the current trend in IoT-driven application scenarios (e.g., water-quality monitoring, flooding prevention, etc.), which often require (shorter) links at near-shore with antennas relatively close to the surface [29], [30]. These different implementation settings imply tides can induce changes in the water level that are in the order of magnitude of the antenna height, possibly intensifying tidal fading and other propagation effects. Although being addressed by a few works in [25], [26], [27], [29], [31], and [32], this issue has been largely ignored in practice and thus represents one of the main targets of our research.

B. Intertidal Zones

Tidal environments such as estuaries and their surrounding wetlands offer distinctive water dynamics (e.g., due to shallow water tides or intertidal zones) that deserve dedicated RF propagation studies. Specifically, the *intertidal zone*, that is, the area within the (estuarine) shoreline that is submerged by water during the high tide and then becomes unveiled during the low tide [16], may pose difficult challenges to channel modeling and characterization. Though a few works have already demonstrated their impact on different aspects of wireless communications (e.g., link quality estimation [33], energy consumption [34], or time synchronization [35]), these prior works considered communicating nodes deployed at the ground level, which become covered by water during the high tide, in contrast to our research. These works offer little insights into the path-loss dynamics occurring *above* in the intertidal zone, which is our major concern.

C. RF Propagation Over Mixed Water/Land Paths

The case of intertidal zones entails a challenging and unusual condition for channel modeling, which is to have a dynamic water/land portion along the link path continuously changing according to the tide. This situation, as far as we know, has been addressed only partially by a few works modeling RF signal propagation over the so-called mixed water/land paths [36], [37], [38], [39]. While these works show ideas resembling our geometrical analysis of the direct and reflected ray using different reflection coefficients depending on where the reflection occurs, they did not consider important challenges such as tidal fading or intertidal zones. The work in [38] assumes that the river level can take different values along the day, thus having an effect on the radio modeling. Still, their analysis focused on a kilometric link using antennas of up to 200-m high, in contrast to our research.

By comparison, our work is more general and challenging since targeting path-loss modeling over dynamic mixed water/land paths that change their physical properties during the day depending on the tide, for example, from a relatively flat (water) surface with varying levels to a possibly rough (soil) surface of varying moisture and specific terrain profile. Without loss of generality, this could be applied to different types of tide-induced environments for which tides and bathymetry are known.

III. METHODOLOGY

This section introduces our novel methodology for modeling large-scale fading of (LoRa) RF links operating over tidal environments. The proposed framework considers: 1) the precise and location-dependent hydrodynamic modeling of the water environment (see Section IV) and 2) the physical and geometrical basis of the two-ray propagation model (see Section V) as building blocks that when integrated improve path-loss estimation. As stated previously, our methodology captures: 1) spatial (height, distance); 2) temporal (over-time tidal dynamics); and 3) physical (terrain profile, permittivity) features of the RF signal interaction with the environment and integrates them into the two-ray propagation model.

More concretely, our methodology takes a step forward on the existing research by simultaneously addressing the following shortcomings.

1) *Spatial variability:* Typically, tidal data are available for a subset of key spots only (e.g., ports, harbors). However, water-level estimations can differ significantly even between two close locations due to local dynamics, being more pronounced in shallow and border waters.
2) *Low temporal resolution:* In general, publicly available tidal data provide only estimates on the so-called *high water* and *low water* levels (usually four samples per day), which, although useful for some general activities, are insufficient for accurately describing complex tidal dynamics at specific locations (e.g., estuaries).
3) *Varying reflecting surface:* Assuming that the secondary ray always reflects on the water can impact the estimation precision of the signal received power. In a realistic scenario, the reflection point can vary between the high and the low tide, especially if links are over an intertidal zone. This implies the reflection surface can change from water to wet/dry soil as a result of the tide.

Consequently, our methodology includes components for: 1) increasing both temporal and spatial resolution of tidal data and 2) accounting for a reflective surface of varying altitude and permittivity as a function of the tide, providing a seamless integration of the tidal and two-ray models. To the best of our knowledge, this integration has not been proposed by any other work in the literature.

The proposed methodology is depicted in Fig. 1. The function of each major component is detailed in the following.

1) *Tidal model:* Bathymetry and other input data (summarized in Table I) are foundational for the construction of the tidal model. They allow to obtain precise

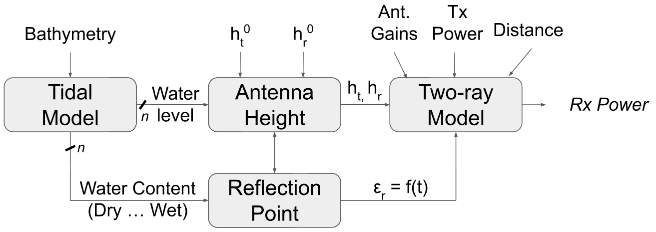

Fig. 1. Proposed methodology for path-loss prediction and its major building blocks.

hydrodynamic outputs, particularly: 1) the water level[2] or the altitude of the soil surface and 2) the associated water content, to be used in the following components of this methodology.

2) *Antenna height:* The water-level estimation and the nominal heights of the receiver (Rx) and transmitter (Tx) antennas with respect to the water level at the high tide (h_r^0 and h_t^0, respectively) are the inputs of this component. They are used to obtain the (relative) antenna heights (with respect to the reflecting surface) to be used by the two-ray model, specifically, h_r and h_t. As shown in Fig. 1, this component also represents a recursive input for the computation of the reflection point.
3) *Reflection point:* The water content allows us to know if the reflection will happen on water or on dry/wet soil. This, in turn, enables the computation of the relative antenna heights, as well as the specific relative permittivity (ε_r) of the reflective medium, which are the two main tide-driven inputs for the two-ray model.
4) *Two-ray model:* Both static (e.g., Tx power) and varying (e.g., ε_r) parameters are then used to determine the main output of the methodology, that is, the Rx power. This main output is equivalent to the average path loss, which here is computed as a consequence of a tide-shifted reflection point of time-varying tidal/terrain data and permittivity.

To the best of our knowledge, this nontrivial integration between precise hydrodynamic and RF propagation modeling represents the first tide-informed methodology for path-loss prediction in overwater RF links deployed over characteristic intertidal zones.

IV. TIDAL DYNAMICS

A. Preliminaries

The sea level in large bodies of water is determined in great measure by the *variable* gravitational forces of both the Moon and the Sun, and the rotation of the Earth [16]. Tides are the result of the influence of those conditions and other astronomical factors (e.g., lunar declination and lunar orbit), which then combine with further phenomena, for example, of meteorological nature (e.g., high/low barometric pressure, wind, and storms) to determine the recurrent rise and fall of the sea level. Still, at some specific locations, for example, rivers, estuaries, or sea coasts, tides exhibit patterns of higher complexity depending, among other details, on the geographical characteristics of the environment. This situation makes variations of the water level in open waters, for example, oceans, clearly different than those at in-land locations, for example, in narrow (estuarine) channels.

TABLE I

MAIN METHODOLOGY INPUTS AND OUTPUTS FOR THE HYDRODYNAMIC (BAROCLINIC MODE) AND TWO-RAY MODELS. FOR THE TIDAL MODEL, THE NUMBER OF INPUTS/OUTPUTS IS REDUCED WHEN SIMULATING FOR BAROTROPIC APPLICATIONS (*: OPTIONAL FIELD)

Model	Type	Data
Hydrodynamic	Input	**bathymetry**, atmospheric data (atmospheric pressure, humidity, wind, air temperature*, downwards/longwave shortwave radiation*), river boundary conditions (flow, salinity*, water temperature*), ocean boundary conditions (tides, salinity, water temperature)
	Output	**water level**, velocity, salinity*, water temperature*
Two-ray	Input	varying **antenna heights** (h_t, h_r) and varying **reflection coefficient** (ϵ_r), static parameters (e.g. tx power, distance)
	Output	Rx Power

To better understand sea-level processes, tidal data are generally obtained from a limited set of *tidal gauges* that record deviations of the water level with respect to a given reference. In general, tidal gauge data are publicly available given their usefulness for several maritime activities (e.g., navigation or habitat protection). However, they typically exhibit poor temporal and spatial resolution, thus being insufficient to properly characterize locations with complex tidal dynamics (e.g., estuaries). For this reason, this work resorts to high-resolution tidal data obtained from hydrodynamic modeling, which have been previously calibrated and validated using field data.

B. Tidal Model

The dynamics of estuarine and coastal waters were simulated using the system of models termed *Semi-implicit Cross-scale Hydroscience Integrated System Model* (SCHISM) [40] in the 3-D baroclinic mode. SCHISM aims at the simulation of surface water processes across estuary/river to ocean scales. The model uses highly efficient and precise semi-implicit finite-element and finite-volume methods, combined with Eulerian–Lagrangian methods, to solve the shallow water equations. The model is based on unstructured grids in the horizontal dimension. In the vertical dimension, the model uses hybrid coordinates, combining terrain-following coordinates (sigma or S) and geo-potential coordinates (Z), or Localized Sigma Coordinates with Shaved Cell (LSC^2) [41]. The simulation also includes wetting and drying of tidal flats. SCHISM can be run in an operational mode using the Water Information Forecast Framework (WIFF) [42], [43] and as part of the OPENCoastS service [44]. The simulation outputs include hydrodynamics and water quality forecasts for the next 48 h. Within the context of this work, the main simulation output provided by the tidal model is summarized in Table I.

1) Model Limitations: Despite its advantages, the tidal model still presents some limitations. First, the model resorts to

---

[2] The water level also provides the water content as a value of −99 means that the sampling point is dry.

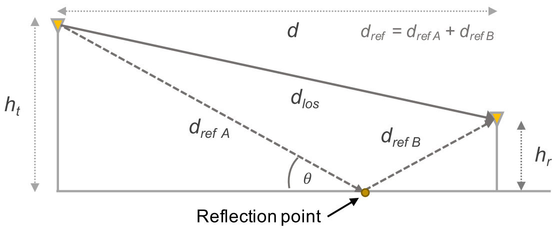

Fig. 2. Classical two-ray model showing: 1) the direct LoS path and 2) the ray reflected on the surface.

bathymetric data provided by the Portuguese Hydrographic Institute from various sources and different time periods. This implies, for example, that bathymetric data might be outdated due to morphological changes (e.g., induced by currents). Second, bathymetric data provide the terrain model for the simulation, thus they determine the accuracy of the provided results. For example, for this test site, bathymetric data have limited spatial resolution (only 100 m), being last acquired in the year 2009. Lastly, the calibration of shallow water constituents (e.g., M_4) may present higher errors, both because of lower predictability and bathymetric imprecision.

V. TWO-RAY CHANNEL MODEL

This section revisits the two-ray propagation model from the perspective of S2S and S2V RF communication links subject to variations in the water surface level. A similar analysis has been presented before in [23], [24], [25], [26], and [27], but using a simplified version of the two-ray model, and without considering the impact of the intertidal zone. Thus, this section also discusses the geometrical aspects of determining whether the reflection point (from the two-ray model viewpoint) falls within the intertidal zone, and how this situation may influence the modeling approach.

A. Classical Two-Ray Model

The two-ray model [17] describes the average path-loss trend (or equivalently, the received power if the transmission power is known) of a link assuming a multipath effect dominated by a single surface reflection. This implies that the received signal strength (RSS) is computed as the vectorial summation of two copies of the transmitted signal that simultaneously arrive at the Rx following two different paths. The first ray follows a direct LoS path between the Tx and the Rx, and the second indirect path is reflected by the surface (see Fig. 2). Note that the length of the reflected ray ($d_{\text{ref}} = d_{\text{ref}A} + d_{\text{ref}B}$) is longer than the length of the direct path (d_{los}), and thus a phase shift $\Delta_\phi = 2\pi(d_{\text{los}} - d_{\text{ref}})/\lambda$ exists between the two copies of the received signal, where $\lambda = c/f$ is the wavelength, c the speed of light, and f is the operating frequency. Formally, the two-ray model can be expressed in terms of the average received power P_r [17] as in the following equation:

$$P_r = P_t G_t G_r \left[\frac{\lambda}{4\pi d}\right]^2 \left|\frac{1}{d_{\text{los}}} + \Gamma \frac{e^{-j\Delta_\phi}}{d_{\text{ref}}}\right|^2 \tag{1}$$

where P_t is the transmit power and G_t and G_r are the Tx and Rx antenna gains, respectively.

TABLE II
TWO-RAY MODEL GEOMETRY WHEN INCORPORATING Δ_h

Variable	Shore-to-Shore (S2S)	Shore-to-Vessel (S2V)
h_t	$h_t + \Delta_h$	$h_t + \Delta_h$
h_r	$h_r + \Delta_h$	h_r
θ	$\arctan\left(\frac{(h_t+\Delta_h)\ (h_r+\Delta_h)}{d}\right)$	$\arctan\left(\frac{(h_t+\Delta_h)\ h_r}{d}\right)$
d_{los}	$\sqrt{d^2 + (h_t - h_r)^2}$	$\sqrt{d^2 + (h_t - h_r + \Delta_h)^2}$
d_{ref}	$\sqrt{d^2 + (h_t + h_r + 2\Delta_h)^2}$	$\sqrt{d^2 + (h_t + h_r + \Delta_h)^2}$
RP	$d\left(1 - \frac{h_t+\Delta_h}{h_t+h_r+2\Delta_h}\right)$	$d\left(1 - \frac{h_t+\Delta_h}{h_t+h_r+\Delta_h}\right)$

The parameter Γ is the Fresnel reflection coefficient given by the following equation:

$$\Gamma = \frac{\sin(\theta) - Z}{\sin(\theta) + Z}. \tag{2}$$

The parameter Z is given by the following equation:

$$Z = \begin{cases} \sqrt{\varepsilon_r - \cos^2\theta}/\varepsilon_r, & \text{for vertical polarization} \\ \sqrt{\varepsilon_r - \cos^2\theta}, & \text{for horizontal polarization} \end{cases} \tag{3}$$

where ε_r is the relative permittivity or dielectric constant of the reflective medium (e.g., ground or water) and θ is the angle of incidence of the ray reflected from the surface.

From simple geometry, the angle θ can be computed using the following equation:

$$\theta = \arctan\left(\frac{h_t + h_r}{d}\right) \tag{4}$$

where d is the horizontal link distance and h_t and h_r denote the Tx and Rx antenna heights, respectively.

Similarly, the path lengths d_{los} and d_{ref} can be calculated with the following equations:

$$d_{\text{los}} = \sqrt{d^2 + (h_t - h_r)^2} \tag{5}$$
$$d_{\text{ref}} = \sqrt{d^2 + (h_t + h_r)^2}. \tag{6}$$

B. Two-Ray Model Over Tidal Waters

From the two-ray model perspective, the rise and fall of water levels will impact the link geometry whenever at least one of the (relative) antenna heights to the surface is modified by the impact of tides [25], [26], [27]. This can be interpreted as the influence of a water-level variation Δ_h that shifts either h_t, h_r, or both, depending on whether it is an S2S or an S2V link scenario, as shown in Fig. 3(a) and (b), respectively. This, in turn, implies the angle of incidence and the lengths of the two-ray paths, that is, θ, d_{los}, and d_{ref}, can also vary as a consequence of tides (Δ_h), but differently for each scenario, as follows.

1) Shore-to-Shore: In this case, both Tx and Rx nodes are assumed as static onshore. This presumes the $\pm|\Delta_h|$ variations on the water-level (along the link path) shift both height terminals simultaneously, and by the same shift amount. This implies Δ_h induces variations on the values of θ and d_{ref}, but not on d_{los}, which remains unchanged due to the shifts getting canceled after incorporating them into the expression of d_{los} (see Table II).

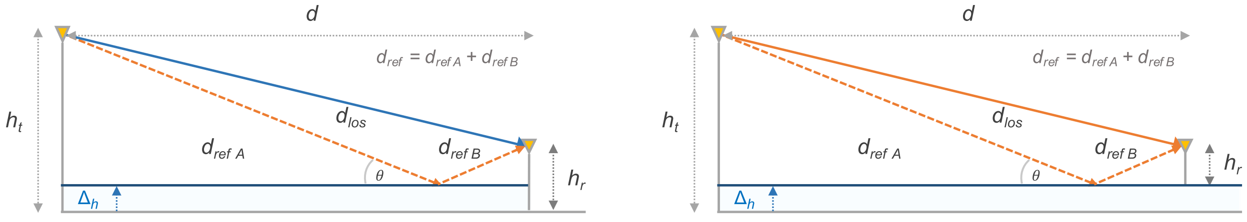

(a) (b)

Fig. 3. Two-ray model geometry for (a) S2S and (b) S2V link scenarios when influenced by a water-level variation of Δ_h. Both pictures are highlighted in orange, the corresponding direct and/or indirect rays being influenced by the water-level shift.

2) Shore-to-Vessel: In this case, only one of the nodes is onshore, while the other is on water (e.g., a vessel or buoy). This implies Δ_h only influences the relative height of the onshore antenna h_t, but not h_r that remains constant with respect to the water surface.[3] This, in turn, induces variations on all the geometrical parameters of the link, that is, θ, d_{los}, and d_{ref}, in contrast with the S2S case.

C. Reflection Point Over Tidal Waters

The reflection point is a fundamental concept in the two-ray model geometry being defined as the distance with respect to the Rx side at which the second ray touches the reflective surface (see Fig. 2). This concept is often left aside from conventional discussions on two-ray propagation modeling since typically invariant, given the common assumption of having a flat and static (ground) reflecting surface. Formally, it can be computed with the following equation:

$$\text{RP} = d\left(1 - \frac{h_t}{h_t + h_r}\right) \tag{7}$$

where d is the link distance, and h_t and h_r are, respectively, the Tx and Rx antenna heights.

For the case of RF links over tidal waters, (7) can be trivially extended by considering either h_t, h_r, or both, being affected by a water-level variation Δ_h depending on whether it is an S2S or S2V link scenario, as summarized in Table II.

D. Reflection Point Falling Within the Intertidal Zone

When the RF links are deployed over tidal environments, the reflection point may fall within the intertidal zone. This implies a dual condition for the reflection point, which is the possibility of falling on: 1) **water** or 2) **soil** as a function of the tide. While the former case is equivalent to the one summarized in Table II, the latter imposes a static definition that may not necessarily fall on flat terrain nor a surface of the same altitude as the average water level in the estuary. This not only influences the geometry, but also the dielectric properties of the composite medium (e.g., permittivity), which do not present a constant behavior throughout the day [45], [46], [47], but vary depending on the floods and ebbs.

The overall situation entails extra considerations on the two-ray channel modeling, which have not been addressed by conventional approaches. For this purpose, this work resorts to the precise hydrodynamic modeling of the specific location (i.e., local tide estimations), which reports not only average water levels along the link path, but also terrain profile (bathymetry) and water content estimations (e.g., dry/wet) at the reflection point. The bathymetric data is used here to estimate the relative shift on the antenna height(s), that is, equivalent to Δ_h, but computed based on the terrain profile differences. The water content, in turn, is used to estimate the relative permittivity of the medium (e.g., $\varepsilon_r = 81$ for water, or $\varepsilon_r = 4$ for ground), but assuming an exponential transition between dry soil and water (or water-saturated soil), as reported in [45]. Note this approach is consistent with the concept of penetration depth [47] that determines the thickness of the medium layer (e.g., minimum water level) required to keep a constant medium dielectric constant. Particularly, the penetration depth for RF signals at 868 MHz is about 10 cm according to [47].

VI. EXPERIMENTAL MEASUREMENTS

A. Setup

We evaluate *S2S* and *S2V* LoRa links operating in a real-world aquatic environment. We used commercial-off-the-shelf (COTS) LoRa radios, namely a Raspberry Pi Dragino hosting an SX1276 chipset. Each radio was coupled to a vertically positioned omnidirectional antenna operating in the 868-MHz RF band. The antennas had nominal gains of 1.5 and 1 dBi for the gateway and end nodes, respectively. All radios were configured using the same system parameters: 1) transmit power of 14 dBm (maximum allowed value in the EU); 2) spreading factor (SF)[4] of 12; 3) coding rate of 4/5; and 4) bandwidth of 500 kHz. The SF was set to maximum for improved communication range, despite the lower resulting data rate, higher channel usage (i.e., higher time-on-air), and increased energy consumption.

In LoRa communications, the selection of a higher bandwidth results in lower Rx sensitivity. Fig. 4 depicts the relationship between the signal-to-noise ratio (SNR) and RSS indicator (RSSI) for different nodes and measurement intervals, revealing that the effective sensitivity of the Rx was about −94 dBm, despite its nominal value of −148 dBm. This result also shows that: 1) the SNR–RSSI relationship holds true for different devices; 2) the SNR is fairly stable at about 9 dB for

---

[3] Note that the Tx–Rx convention defining the Tx onshore and the Rx on water (or vice versa) is arbitrary, and thus, it does not impact the geometry.

[4] SF is defined as the ratio between chip rate and the symbol rate.

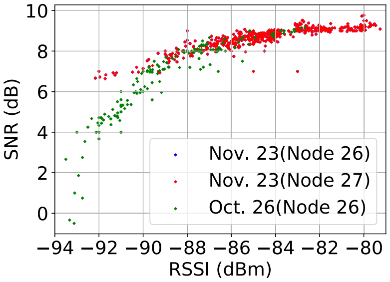

Fig. 4. Relationship between SNR and RSSI for three different nodes. It shows the effective sensitivity of the Rx is about −94 dBm for all devices.

the RSSI interval [−85, −79] dBm; and 3) there is an abrupt decrease in the SNR for RSSI values lower than −88 dBm. These observations are relevant for a better understanding of the results presented in Section VII.

Both gateway and end nodes were kept static during the experiments. The gateway was placed onshore at a fixed height of 3.2 m from the ground. The (relative) height of the gateway with respect to the water surface varied along the day according to tide dynamics. A minimum height to the water of 4 m was measured during the high tide period. For both link scenarios, the gateway was kept at the same position, that is, at (38°37’46.9”N 9°06’19.2”W). The end nodes were installed in two different structures: 1) a portable mast pole placed at (38°37’52.3”N 9°06’49.6”W) and 2) a floating platform at (38°37’52.8”N 9°06’49.5”W). The mast pole and the floating platform structures are shown in Fig. 5(a) and (b), respectively, and described in more detail next.

1) *Mast pole (S2S Link):* One node was installed on a temporary wood pole at a nominal height of 1.5 m with respect to the water surface, measured during the high tide. The effective height varied throughout the whole tidal cycle as a function of the water level.
2) *Floating platform (S2V Link):* Two nodes were installed at ∼15 m from the entrance of a docking pier, having been attached to an existing metal structure. The docking pier has about 75 m of length and a slight inclination due to the terrain profile. The nominal heights of the two nodes, 0.5 and 1.5 m, were measured during the high tide with respect to the water surface. The platform floated after a given tide-level threshold and sat on the land/mud otherwise. The effective height of nodes was thus constant when the platform was floating, but varied according to the tide the rest of the time.

GPS devices were used in all nodes for the purpose of accurate positioning and timekeeping. The link distance was computed based on the Tx–Rx separation using the median of the GPS coordinates. The resulting distance was approximately 740 and 750 m for the S2S and S2V link scenarios, respectively.

B. Measurement Site

The experiments were carried out in the southern part of the Estuary of the Tagus River, Portugal, one of the largest estuaries in Europe with an area of about 320 km^2. The Tagus Estuary connects to the Atlantic ocean through a deep, long, and narrow inlet. Specifically, the measurement campaigns were performed at the Bay of Seixal on 26 October 2019 (08:20 A.M. to 19:02 P.M.) and 23 November 2019 (06:32 A.M. to 16:07 P.M.). Measurements included both complete flooding and ebb periods. The maximum width of the bay is approximately 750 m. The bay is surrounded by a promenade for recreational, commercial, and industrial activities. Both S2S and S2V scenarios were deployed across the estuary with link paths occurring over the intertidal zone. The Tx and the Rx were predominantly in LoS conditions, although a low number of surrounding static and mobile objects (e.g., boats) were present during the measurements. For the subsequent analysis, we only considered data transmission between the gateway and the end nodes, assuming a strong degree of link reciprocity [48].

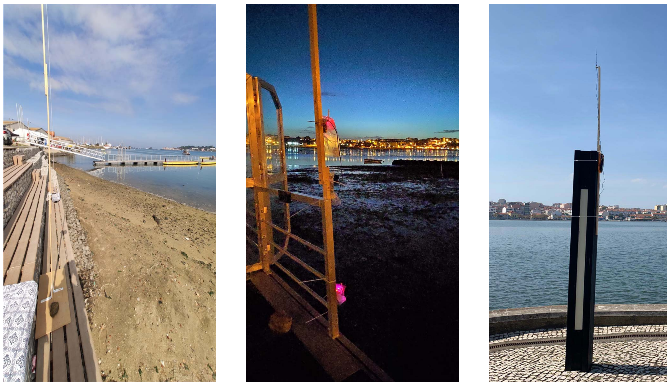
(a) (b) (c)

Fig. 5. Measurement setup and installation locations for (a) and (b) end nodes, and (c) gateway for the campaigns conducted on 26 October 2019 and 23 November 2019.

C. Measurement Protocol

To perform the link quality measurements, a *request–reply* protocol was implemented in both terminals. For improved energy efficiency, the protocol considered a 5-min *measurement phase* interleaved with a *stand-by phase* with 10-min duration. During the measurement phase, the radios transmitted packets with an average size of 85 bytes every ∼2 s, with requests being triggered by the gateway. The gateway stored the messages received by itself and by the end nodes, included as part of the end node’s *reply* message. Specifically, the following timestamped metrics were recorded: 1) packet RSSI; 2) SNR; and 3) packet sequence number (SN). The SNs were used to identify gaps in packet transmission allowing us to determine the packet delivery ratio (PDR) during a given time interval. The metrics were stored in logs for subsequent processing.

D. Tidal Dynamics in the Tagus Estuary

Water circulation in the Tagus estuary is mainly driven by semi-diurnal tides. Other effects (e.g., atmospheric pressure, wind, river flow, or surface waves) also affect the circulation within the estuary, especially during storms [18]. Tidal

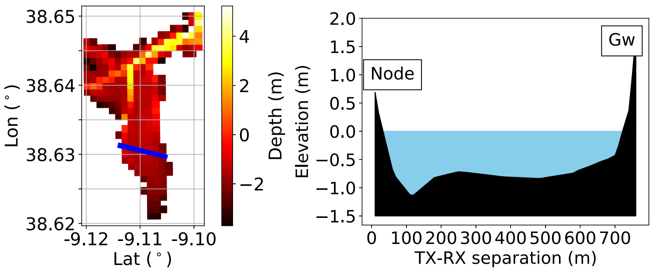

(a) (b)

Fig. 6. (a) Bathymetry data for the Bay of Seixal and (b) one example bathymetric cross section of simulation mesh for communication link of 23 November 2019. The cross section for the other measurement day (26 October 2019) is very similar.

dynamics in the Tagus estuary are complex location-dependent phenomena affected by estuarine coastline features and topography [49], [50]. The tidal range is significantly amplified within the estuary due to resonance effects [49]. To accurately represent all the relevant physical processes, the tidal model includes the whole estuary from the river to the ocean (27 km away from the estuary mouth). The horizontal grid has about 83 000 nodes with a typical resolution of 15–25 m; the vertical domain is discretized with a hybrid grid with 39 SZ levels. The numerical model of the Tagus estuary is forced by:

1) tides, salinity, water temperature, and water quality tracers' concentrations at the **oceanic boundary**;
2) river flows, salinity, water temperature, and water quality tracers' concentrations at the **riverine boundaries** (Tagus and Sorraia rivers); and
3) atmospheric forecasts at the **surface**.

The calibration and validation of the model were performed by comparison with several datasets, including water levels, salinity, water temperature, dissolved oxygen, inorganic nutrients, and chlorophyll-a data. Prior results showed the model's ability to represent the main spatial and temporal patterns of circulation and water quality in the test site [18], [19]. Water-level information is obtained in several (76) sampling points along a cross section of the simulation mesh using a time step of 60 s. Bathymetry data for the Tagus Estuary is depicted in Fig. 6 alongside a given interpolation of the bathymetry mesh along the communication link path between the Tx and the Rx. Further details about the model implementation can be found in [18] and [19].

The LoRa measurements were performed in one of the narrowest and shallowest channels of the Tagus Estuary. As usual, the water level in this location varies according to the tidal cycle. However, the considered test sites are located in a tidal flat region, where **drying** occurs during part of the tidal cycle (i.e., low tide). Note that tides in the Tagus Estuary are predominantly ebb asymmetric due to differences in the ebb and flood duration. Specifically, tides in the Bay of Seixal are even further asymmetric with **ebb dominance**, that is, with the span of the rising tides exceeding the duration of falling tides, causing a net export of sediments of the bay. These specific characteristics of the measurement site (i.e., ebb dominance and drying of the tidal flat during low tides) are important for the analysis of the results in Section VII.

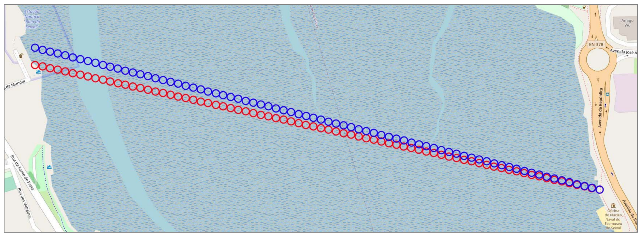

Fig. 7. Tidal model sampling points for the two experiments days represented in red for 26 October 2019 (*S2S link*) and in blue for 23 November 2019 (*S2V link*). The gateway was placed on the right side of the river bank, while the Rx was placed in structures on the left bank of the river.

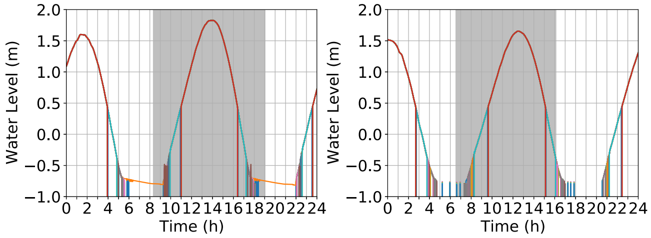

(a) (b)

Fig. 8. Water-level variation with respect to the average level (0 m) for each sampling point throughout the two measurement days, namely 26 October 2019 and 23 November 2019 (different colors per curve; curves overlap). Most of the 76 sampling points are dry during the two low tide periods. The period during which the experiments were carried out is highlighted in gray. (a) S2S link: 26 October 2019. (b) S2V link: 23 November 2019.

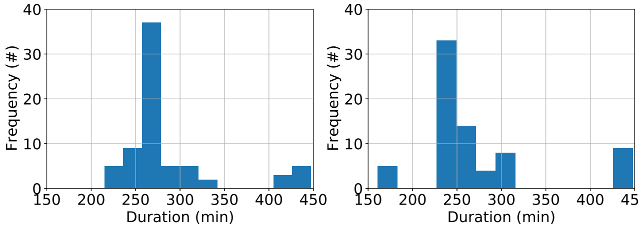

(a) (b)

Fig. 9. Largest time interval between drying and subsequent flood for each of the 76 sampling points, for both measurement days, namely (a) 26 October 2019 and (b) 23 November 2019. Four sampling points are permanently dry, that is, the time interval of 1440 min, but are not herein presented for visual clarity.

VII. RESULTS AND DISCUSSION

A. Tidal Dynamics

Fig. 7 shows an aerial view of both S2V and S2S links containing all the 76 sampling points obtained using the model detailed in Section IV. Each point was obtained by dividing the link path into areas of equal size, that is, 75 areas of ∼10 m, as S2S and S2V links were about 750 and 740 m, respectively.

Each of the 76 sampling points tracks water-level variations along a 24-h period. The data from all these points is shown jointly in Fig. 8, with different colors. The results show that most points differ from others only during low-tide periods, while reporting the same level of water during high tide. The differences that occur during the low-tide period occur mainly due to the terrain profile as explained in more detail later. The water level is given with respect to the average sea level of the

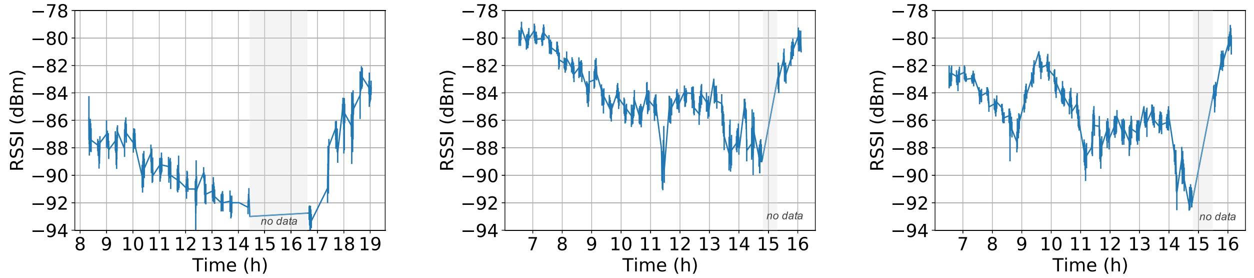

(a) (b) (c)

Fig. 10. RSSI for S2S and S2V link scenarios as a function of time. RSSI data have been aggregated into 1-min bins presenting the mean and standard deviation for each bin. (a) S2S link: 26 October 2019 (node 26). (b) S2V link: 23 November 2019 (node 26). (c) S2V link: 23 November 2019 (node 27).

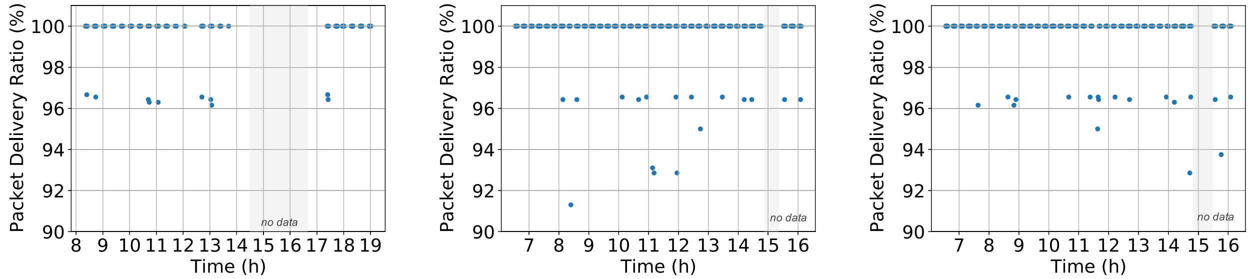

(a) (b) (c)

Fig. 11. PDR for S2S and S2V link scenarios as a function of time. Data have been aggregated into 1-min bins considering at least 15 transmitted packets. (a) S2S link: 26 October 2019 (node 26). (b) S2V link: 23 November 2019 (node 26). (c) S2V link: 23 November 2019 (node 27).

measurement site, that is, 2.26 m above the hydrographic zero of Portugal. The results show a typical pattern for water-level variations with a tidal range of approximately 2.5 m for both measurement days.

The output of the model also shows that drying[5] occurs in this region during the morning and afternoon periods (e.g., 5–10 and 17–22 h for 26 October 2019) for the vast majority of the sampling points. This implies that solely the river banks and the deeper navigation canal of the estuary can be considered covered by water during all times on 26 October 2019. Equivalent reasoning is applicable for the tidal data from 23 November 2019.

Fig. 9 shows the longest time period during which each sampling point was dry, that is, the largest time interval between drying and subsequent flood for each of the 76 sampling points. As expected, some sampling locations become dry earlier and are flooded later depending on the topographical features of the terrain (e.g., elevated terrain parts become dry earlier). The median longest dry duration is 277 and 249 min for 26 October 2019 and 23 November 2019, respectively. These results suggest that the reflecting surface effectively changes along the tidal cycle, from water to soil with different water content (from mud to dry soil).

B. Analysis of Empirical Measurements

1) RSS Indicator: Fig. 10 presents the variation of RSSI as a function of time for both measurement days (26 October 2019 and 23 November 2019), link types (S2S and S2V), and for all nodes (i.e., nodes 26 and 27). The results show a clear impact of the tides on the measured signal power with variations exceeding 10 dB during the measurement span. In broad terms, RSSI decreases/increases as the water level raises/falls, which can be explained by the changes in the effective antenna height to the water surface, which—for the considered Tx–Rx separation—leads to an increase in the signal attenuation as shown in previous studies [31].

As detailed previously, for the S2V case, node 26 [see Fig. 10(b)] and node 27 [see Fig. 10(c)] are installed at the same location but at different heights (0.5 and 1.5 m, respectively). Comparing the RSSI measurements of both nodes the signal strength is, in general, larger for the upper node (i.e., node 26) as expected, although this does not hold true for short periods of time. Recall that these nodes are installed in a floating platform that is *static* during low tide and that *floats* during the high tide, which renders different propagation conditions. As for the S2S case, node 26 [see Fig. 10(a)] exhibits an increasing/decreasing relationship which is in agreement with the tidal influence, and thus with the effective antenna-to-surface heights of the nodes.

2) Packet Delivery Ratio: Fig. 11 depicts the PDR as a function of time for both measurement days, link types, and all nodes. As expected, the PDR is fairly constant at around 100% with occasional packet losses despite the wide variations in RSSI. As shown in Section VI-A, the effective sensitivity of the Rx is around −94 dBm. For the S2S link [see Fig. 11(a)], this implies packets that have been sent between slightly after the 14 h and before 17 h were not received due to the RSSI being below the Rx sensitivity. Similarly, no packets are

---

[5] The tidal model attributes a −99 m water level to a given sampling point whenever drying occurs. This value is not depicted in Fig. 8 for visual clarity.

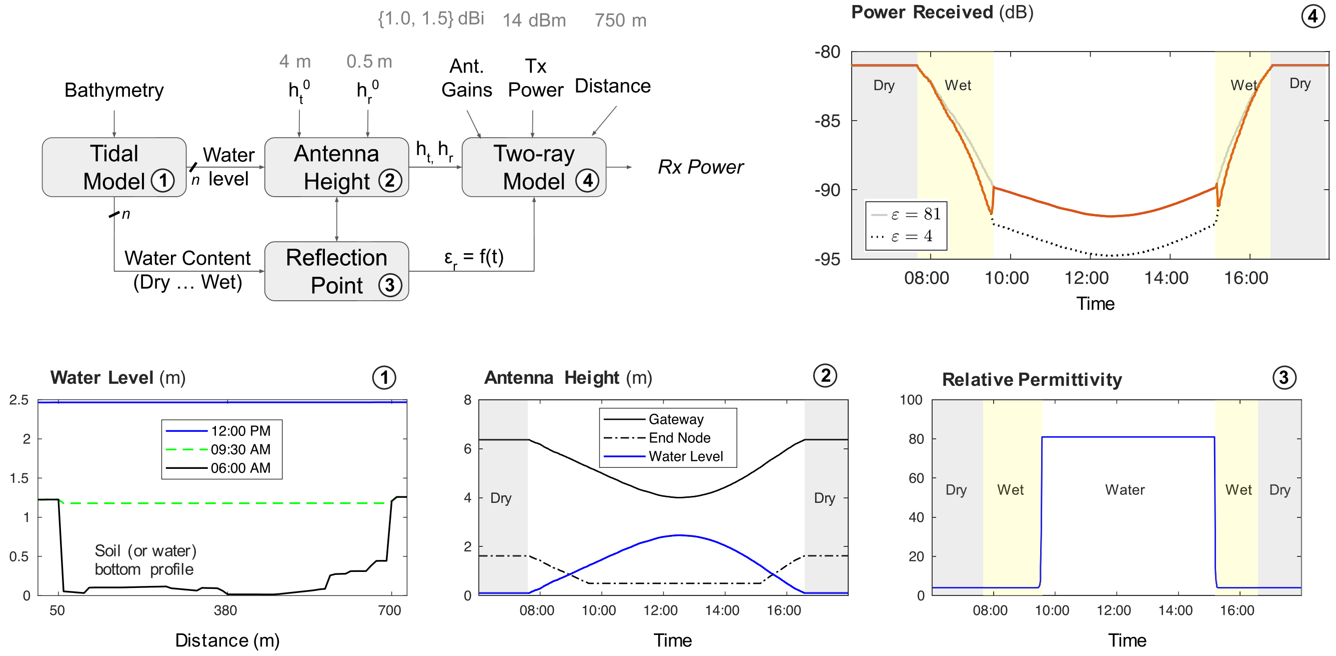

Fig. 12. Illustrative example of the proposed methodology for modeling the RSS of node 26 ($h_r = 0.5$ m) for the S2V measurement campaign of 23 November 2019. The figure includes the intermediate outputs from the tidal model, antenna height, and reflection point stages, as well as the final output.

received for a shorter period of time around 15 h by node 26 [see Fig. 11(b)] and node 27 [see Fig. 11(c)] for the S2V link. Previous works [7], [8], [29], [31] have also shown that LoRa's effective communication range is severely compromised when using antennas close to the surface (water or ground), due to reduced Fresnel zone.

C. Evaluation of the Proposed Methodology

1) Illustrative Example: In the following, we provide an illustrative example of the application of our methodology for determining the received signal power in intertidal scenarios described in Section III. Fig. 12 presents the output of the different blocks of the processing pipeline given in Fig. 1. We focus the analysis on the measurements collected on 23 November 2019 for node 26 (S2V link) as this is the most representative and complete scenario.

The first step of the processing pipeline consists of determining the: 1) *water level* and 2) *water content* (i.e., dry to wet) for each of the 76 sampling points using the calibrated tidal model. The model principles and output (i.e., *tidal dynamics*) are presented in detail in Section VII-A. Fig. 8(b) depicts the water level for 23 November 2019, reporting significant variations in the water content in the different sampling points during the low tide and that during the high tide all sampling points report the same water level as was foreseeable.

Fig. 12 (bottom left) shows the water level along the link path for three different times (6:00 A.M., 09:30 A.M., 12:00 P.M.). This complements the full-cycle water-level variations reported in Fig. 8(b) by highlighting specific instants at the low-tide (6:00 A.M.) and high-tide (12:00 P.M.) periods, as well as the moment slightly before the water reaches the platform (9:30 A.M.), that is, before it starts to float. Note that at the low tide, the curve reports the lowest water level of the basin area or equivalently the model's *soil bottom* as a result of truncating those water content values denoting a dry soil (−99) to the minimum water level (or altitude) of the sampling point. The resulting bottom profile follows a similar trend to the bathymetric cross section in Fig. 6.

In the subsequent step, the Tx/Rx antenna heights are computed using the water-level data provided by the tidal model. The output is calibrated using empirical antenna height measurements (h_t^0 and h_r^0) performed during the high tide. As expected, the antenna height of the onshore Tx (gateway) varied with the tidal cycle decreasing from approximately 6–4 m during the high tide. The height of the Rx was constant at 0.5 m with respect to the water surface while the platform was floating (i.e., between 9:34 and 15:08). After the platform sat on the mud, the antenna height increased to approximately 2 m during the ebb period as a consequence of the currents leading the water mass outside the Bay. Note the Tx and the Rx antenna heights solely vary *simultaneously* during the short transition period between low tide to high tide (7:37–9:34) and vice versa (15:08–16:35). These periods correspond in Fig. 12 (bottom right) to the *wet* areas, in which the reflecting surface passes from a dry soil to water.

In the third step, the relative permittivity (ε_r) of the reflecting medium is determined as a function of a time-varying reflection point. This point has a bidirectional relationship with the resulting Tx and Rx antenna heights from step two (h_t and h_r, respectively) which denote relative height measurements with respect to the soil or water level at the reflection point. The relative permittivity is then computed using data from the specific location at the reflection point,

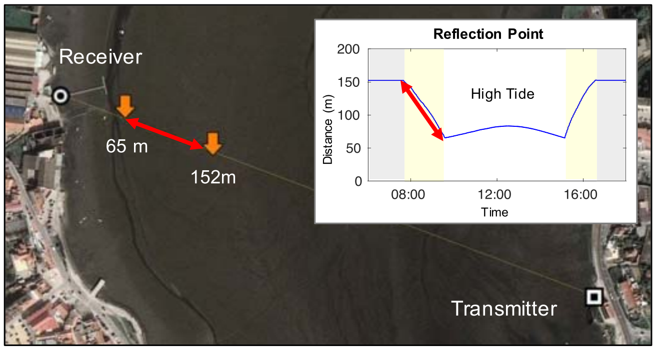

Fig. 13. **Background**. Aerial view of the link path area for the 26 November 2019 campaign, with marks on the maximum and minimum bounds on the reflection point, 65 and 152 m, respectively, for node 26 ($h_r = 0.5$ m). **Box**. Temporal evolution of the reflection point highlighting the distance span.

namely using antenna heights from step two and water content from step one.

Fig. 13 shows an aerial view of the spatial span incurred by the reflection point along the link path for the 23 November 2019 measurement campaign. It also marks the maximum and minimum distance bounds (with respect to the Rx) resulting from the respective low-tide and high-tide peaks on the water level. Recall that the reflection point is geometrically defined, thus computed differently depending on whether it is an S2S or an S2V link scenario, as summarized in Table II.

After determining the point in which the secondary ray reflects, the methodology computes whether the reflection occurs on the water mass or on the bottom terrain of the intertidal zone, which might have a varying water content as this liquid evaporates/infiltrates when the tide is decreasing/increasing, respectively. In this work, we consider the permittivity to be constant whenever the reflection occurs on the ground ($\epsilon_r = 4$) or water ($\epsilon_r = 81$) but showing a varying behavior within the transition area between these two states. Particularly, for improved accuracy, we assume an exponential increase in the value of permittivity with increasing distance from the soil surface, as in [45]. The resulting permittivity curve is depicted in Fig. 12 (bottom right).

The final step consists of determining the average received power using the two-ray model (see Section V) from the time-series data computed in the previous steps and other conventional (static) inputs for path-loss modeling, namely the Tx–Rx distance, Tx power, and antenna gains. The resulting model output shows a clear relation between received power and antenna height variations with lower antenna heights leading to increased signal attenuation. In addition, the transition period between ground reflections to reflection on the water leads to an increase in the received signal power due to the higher permittivity of the water medium.

2) Methodology Validation: Fig. 14 reports the average received power obtained using the methodology described in Section III and the corresponding empirical measurements for the two experimental campaigns. Fig. 14(a) and (b) shows the results for the S2V links of 23 November 2019, when the Rx antennas are at $h_r = 0.5$ and 1.5 m, respectively, measured with respect to the water surface during high tide. Fig. 14(c) shows the results for the S2S case, that is, $h_r = 1.5$ m.

The impact of water level (and corresponding relative antenna heights) on the power received is noticeable in all the evaluated cases, showing increasing/decreasing trends in agreement with the methodological predictions. Particularly, the extreme and central parts of the curves show consistent behavior with the dual condition of the intertidal zone, generally, with higher power received during low tide periods, and thus with more attenuation during the high tide.

The influence of the relative permittivity is substantial in the case depicted in Fig. 14(a), where a rapid shift in the received power is predicted between the $\varepsilon = 4$ and 81 curves, in the central area of the figure. A similar trend but with a larger difference (~5 dB) is exhibited by the experimental measurements. The exponential change of permittivity (see Fig. 12) leading to an abrupt shift up/down on the predicted power received is also similar, but with a less abrupt empirical transition. Fig. 14(b), although corresponding to the same measurement campaign (S2V), shows marginal differences in this effect. Similarly, the results reported for the S2S case in Fig. 14(c) are also negligible.

Further phenomena not explained by our methodology are visible, for example, in Fig. 14(a) and (b), between 11:00 A.M. and 12:00 P.M., and 13:00 P.M. and 15:00 P.M.. A period without data is reported in Fig. 14(c), between around 14:00 P.M., and slightly after 15:00 P.M.. Despite these limitations, trends in the path-loss predictions are, in general, in good agreement with the empirical results. Note that we use the two-ray model for *path-loss* prediction only, thus leaving other propagation effects beyond the scope of this work. To reduce the mismatches between the measured and estimated power, it would be convenient to account for additional factors (e.g., scattering and diffraction) in future work. Although not significant [51], [52] for the comparatively shorter links (750 m) that are the target of this study, tropospheric effects could be included in an extended methodology that considers substantially larger links (i.e., several kilometers) that often exist in aquatic/maritime environments.

Discussion: The proposed methodology requires the use of a hydrodynamic model to simulate the tide. Hydrodynamic model applications are common for estuarine and coastal regions (e.g., [53], [54]) and require a set of inputs such as bathymetric and atmospheric data. Although bathymetric data are available at global and regional scales (e.g., GEBCO global ocean dataset[6] or EMODNet Digital Terrain Model for European Sea regions),[7] these data are often limited at local scales and specific bathymetric surveys might be required for local applications. Recent platforms to generate coastal forecast systems for any location, such as OPENCoastS [44], [55], might also be useful to support the implementation of hydrodynamic models for regions where such applications are not available.

The nontrivial integration of the two-ray path-loss model with the precise estuarine hydrodynamics offers an improved

---

[6] https://www.gebco.net/data_and_products/gridded_bathymetry_data/

[7] https://www.emodnet-bathymetry.eu/data-products

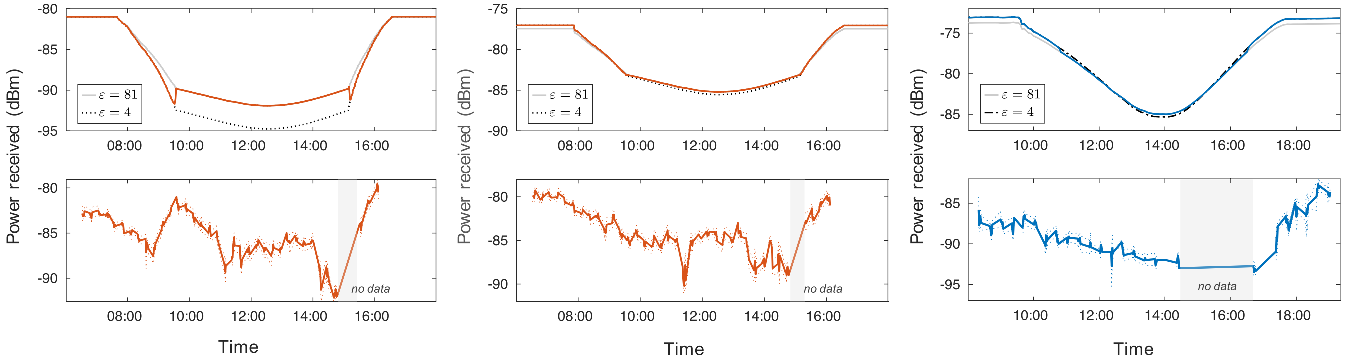

(a) **S2V link:** Nov. 23, 2019 (h_r = 0.5 m) (b) **S2V link:** Nov. 23, 2019 (h_r = 1.5 m) (c) **S2S link:** Oct. 26, 2019 (h_r = 1.5 m)

Fig. 14. Average power received and corresponding experimental measurements for both (a) and (b) S2V, and (c) S2S link scenarios.

estimation of the link quality able to predict RSSI trends and magnitude differences (~5–10 dB) between the low- and high-tide periods that would have not been possible without a tide-informed framework. A naive path-loss estimation (e.g., with the common free-space path-loss model) will not consider antenna heights at all, producing a single RSSI output that only depends on the link distance for the whole measurement span and thus misses the impact of tides. Similarly, an approach based on the two-ray model with tides that do not keep track of the temporal reflection point evolution will not consider the difference between dry, wet, or water permittivity nor the possible terrain profile differences. As observed, this can lead to significant RSSI differences both in modeling and experiments, in this case, up to 10 dB, which justifies the importance of our approach.

VIII. CONCLUSION

This article studies the large-scale fading dynamics of LoRa LoS links deployed over estuaries with characteristic intertidal zones for both S2S and S2V links. We propose a novel methodology for the path-loss prediction that captures spatial (i.e., location-specific water levels), temporal (i.e., time-varying water levels), and physical (varying soil properties) features of the RF signal interaction with the environment, seamlessly integrating those features into the two-ray model. To achieve this with high precision, we coupled a high-resolution hydrodynamic model of the specific location (Tagus Estuary), including the terrain profile (bathymetry) information at the time-evolving reflection point. This aspect is key to accounting for a reflecting surface of varying altitude and permittivity as a function of the tide. Empirical results using LoRa communication devices in the 868 MHz band show that: 1) the RSS decreases/increases more than 10 dB as the water level raises/falls due to changes in the effective antenna height to the water surface and 2) exist notable differences in the S2S and S2V links behavior. Experimental measurements have also demonstrated that major trends of the received power are in agreement with the methodology's prediction.

In future work, we plan to validate the methodology in different surroundings (e.g., harbors and marinas), as well as in other RF communication bands (e.g., 2.4 and 5 GHz). We also intend to include additional propagation effects (e.g., scattering and multipath) and environmental phenomena (e.g., sea waves) into the current modeling framework to further increase the accuracy of link estimation. Additional measurements will also be conducted on consecutive days to characterize possible day-to-day variations of the received signal power as well as to quantitatively assess the quality of our prediction. The end goal is to provide RF practitioners with a network design tool specifically proposed for the deployment of IoT-based environmental systems operating over water environments.

REFERENCES

[1] *Transforming Our World: The 2030 Agenda for Sustainable Development*, United Nations General Assembly, New York, NY, USA, 2015.

[2] O. Khutsoane, B. Isong, N. Gasela, and A. M. Abu-Mahfouz, "WaterGrid-Sense: A LoRa-based sensor node for industrial IoT applications," *IEEE Sensors J.*, vol. 20, no. 5, pp. 2722–2729, Mar. 2020.

[3] Y. Song *et al.*, "Internet of Maritime Things platform for remote marine water quality monitoring," *IEEE Internet Things J.*, vol. 9, no. 16, pp. 14355–14365, Aug. 2022.

[4] U. Raza, P. Kulkarni, and M. Sooriyabandara, "Low power wide area networks: An overview," *IEEE Commun. Surveys Tuts.*, vol. 19, no. 2, pp. 855–873, 2nd Quart., 2017.

[5] J. Petajajarvi, K. Mikhaylov, A. Roivainen, T. Hanninen, and M. Pettissalo, "On the coverage of LPWANs: Range evaluation and channel attenuation model for LoRa technology," in *Proc. 14th Int. Conf. ITS Telecommun. (ITST)*, Dec. 2015, pp. 55–59.

[6] Z. Zhang, S. Cao, and Y. Wang, "A long-range 2.4 G network system and scheduling scheme for aquatic environmental monitoring," *Electronics*, vol. 8, no. 8, p. 909, 2019.

[7] L. Parri, S. Parrino, G. Peruzzi, and A. Pozzebon, "Low power wide area networks (LPWAN) at sea: Performance analysis of offshore data transmission by means of LoRaWAN connectivity for marine monitoring applications," *Sensors*, vol. 19, no. 14, p. 3239, Jul. 2019.

[8] Y. Wang, X. Zheng, L. Liu, and H. Ma, "PolarTracker: Attitude-aware channel access for floating low power wide area networks," in *Proc. IEEE Conf. Comput. Commun.*, Apr. 2021, pp. 1–10.

[9] L. Baghel, S. Gautam, V. Malav, and S. Kumar, "TEMPSENSE: LoRa enabled integrated sensing & localization solution for water quality monitoring," *IEEE Trans. Instrum. Meas.*, vol. 71, pp. 1–11, 2022.

[10] D. Taplin, "Tidal fading on short oversea paths elliptical, vertical and horizontal polarisation compared," NASA, Washington, DC, USA, Tech. Rep., 1975, p. 15328.

[11] A. Mondloch, "Overwater propagation of millimeter waves," *IEEE Trans. Antennas Propag.*, vol. AP-17, no. 1, pp. 82–85, Jan. 1969.

[12] M. Pereira, "Spread spectrum techniques in wireless communication part 2: Transmission issues in free space," *IEEE Instrum. Meas. Mag.*, vol. 13, no. 1, pp. 8–14, Feb. 2010.

[13] G. Bernardi, P. Buneman, and M. K. Marina, "Tegola tiered mesh network testbed in rural Scotland," in *Proc. ACM Workshop Wireless Netw. Syst. Developing Regions*, Oct. 2008, pp. 9–16.

[14] C.-W. Ang and S. Wen, "Signal strength sensitivity and its effects on routing in maritime wireless networks," in *Proc. 33rd IEEE Conf. Local Comput. Netw. (LCN)*, Oct. 2008, pp. 192–199.

[15] Y. Huo, X. Dong, and S. Beatty, "Cellular communications in ocean waves for maritime Internet of Things," *IEEE Internet Things J.*, vol. 7, no. 10, pp. 9965–9979, Oct. 2020.

[16] D. Pugh and P. Woodworth, *Sea-Level Science: Understanding Tides, Surges, Tsunamis and Mean Sea-Level Changes*. Cambridge, U.K.: Cambridge Univ. Press, 2014.

[17] A. Goldsmith, *Wireless Communications*. Cambridge, U.K.: Cambridge Univ. Press, 2005.

[18] M. Rodrigues and A. Fortunato, "Assessment of a three-dimensional baroclinic circulation model of the Tagus estuary (Portugal)," *AIMS Environ. Sci.*, vol. 4, no. 6, pp. 763–787, 2017.

[19] M. Rodrigues *et al.*, "A web-based observatory for biogeochemical assessment in coastal regions," *J. Environ. Informat.*, vol. 38, no. 1, pp. 1–15, 2021.

[20] J. Wang *et al.*, "Wireless channel models for maritime communications," *IEEE Access*, vol. 6, pp. 68070–68088, 2018.

[21] W. Chen *et al.*, "A survey of maritime communications: From the wireless channel measurements and modeling perspective," *Regional Stud. Mar. Sci.*, vol. 48, Nov. 2021, Art. no. 102031.

[22] G. M. Bianco, R. Giuliano, G. Marrocco, F. Mazzenga, and A. Mejia-Aguilar, "LoRa system for search and rescue: Path-loss models and procedures in mountain scenarios," *IEEE Internet Things J.*, vol. 8, no. 3, pp. 1985–1999, Feb. 2021.

[23] A. Macmillan, M. K. Marina, and J. T. Triana, "Slow frequency hopping for mitigating tidal fading on rural long distance over-water wireless links," in *Proc. INFOCOM IEEE Conf. Comput. Commun. Workshops*, Mar. 2010, pp. 1–5.

[24] N. Fuke, K. Sugiyama, and H. Shinonaga, "Long-range oversea wireless network using 2.4 GHz wireless LAN installation and performance," in *Proc. Int. Conf. Comput. Commun. Netw. (ICCCN)*, Oct. 2003, pp. 351–356.

[25] M. G. Gaitan, L. Pinto, P. M. Santos, and L. Almeida, "On the two-ray model analysis for overwater links with tidal variations," in *Proc. Nat. Symp. Informat. (INFORUM)*, 2019, pp. 1–7.

[26] M. G. Gaitan, P. M. Santos, L. Pinto, and L. Almeida, "Optimal antenna-height design for improved capacity on over-water radio links affected by tides," in *Proc. Global OCEANS*, Oct. 2020, pp. 1–7.

[27] M. G. Gaitan *et al.*, "Wireless radio link design to improve near-shore communication with surface nodes on tidal waters," in *Proc. OCEANS*, Sep. 2021, pp. 1–8.

[28] Y.-M. Le Roux, J. Ménard, C. Toquin, J.-P. Jolivet, and F. Nicolas, "Experimental measurements of propagation characteristics for maritime radio links," in *Proc. Int. Conf. Intell. Transp. Syst. Telecommun. (ITST)*, Oct. 2009, pp. 364–369.

[29] G. Callebaut and L. Van der Perre, "Characterization of LoRa point-to-point path loss: Measurement campaigns and modeling considering censored data," *IEEE Internet Things J.*, vol. 7, no. 3, pp. 1910–1918, Mar. 2020.

[30] A. Gutiérrez-Gómez *et al.*, "A propagation study of LoRA P2P links for IoT applications: The case of near-surface measurements over semitropical rivers," *Sensors*, vol. 21, no. 20, p. 6872, 2021.

[31] J. Cecílio, P. M. Ferreira, and A. Casimiro, "Evaluation of LoRa technology in flooding prevention scenarios," *Sensors*, vol. 20, no. 14, p. 4034, 2020.

[32] M. G. Gaitan, P. M. Santos, L. R. Pinto, and L. Almeida, "Experimental evaluation of the two-ray model for near-shore WiFi-based network systems design," in *Proc. IEEE 91st Veh. Technol. Conf.*, May 2020, pp. 1–3.

[33] X. Zhou, X. Ji, Y.-C. Chen, X. Li, and W. Xu, "LESS: Link estimation with sparse sampling in intertidal WSNs," *Sensors*, vol. 18, no. 3, p. 747, 2018.

[34] X. Zhou, Y. Li, D. He, C. Zhang, and X. Ji, "Energy-efficient channel allocation based data aggregation for intertidal wireless sensor networks," *IEEE Sensors J.*, vol. 21, no. 15, pp. 17386–17394, Aug. 2021.

[35] M. Xu and W. Xu, "TACO: Temperature-aware compensation for time synchronization in wireless sensor networks," in *Proc. IEEE 10th Int. Conf. Mobile Ad-Hoc Sensor Syst.*, Oct. 2013, pp. 122–130.

[36] A. Braga *et al.*, "Radio propagation models based on machine learning using geometric parameters for a mixed city-river path," *IEEE Access*, vol. 8, pp. 146395–146407, 2020.

[37] A. Macedo *et al.*, "Mixed path model for urban and suburban city-river path for 1,400 MHz," in *Proc. IEEE Int. Microw. Optoelectron. Conf.*, Nov. 2019, pp. 1–3.

[38] T. da Silva, A. Costa, D. da Silva, L. Castro, J. Araujo, and G. Cavalcante, "Radio propagation for the Amazon region considering the river level," in *Proc. Workshop Commun. Netw. Power Syst. (WCNPS)*, Oct. 2019, pp. 1–4.

[39] L. Carter, "UHF propagation over a cluttered, mixed land/water path," in *Proc. 6th Int. Conf. Mobile Pers. Commun.* Edison, NJ, USA: IET, 1993, pp. 1–6.

[40] Y. J. Zhang, F. Ye, E. V. Stanev, and S. Grashorn, "Seamless cross-scale modeling with SCHISM," *Ocean Model.*, vol. 102, pp. 64–81, Jun. 2016.

[41] Y. J. Zhang, E. Ateljevich, H.-C. Yu, C. H. Wu, and J. C. Yu, "A new vertical coordinate system for a 3D unstructured-grid model," *Ocean Model.*, vol. 85, pp. 16–31, Jan. 2015.

[42] A. B. Fortunato *et al.*, "Operational forecast framework applied to extreme sea levels at regional and local scales," *J. Oper. Oceanogr.*, vol. 10, no. 1, pp. 1–15, 2017.

[43] J. Rogeiro *et al.*, "Running high resolution coastal models in forecast systems: Moving from workstations and HPC cluster to cloud resources," *Adv. Eng. Softw.*, vol. 117, pp. 70–79, Mar. 2018.

[44] A. Oliveira *et al.*, "Forecasting contrasting coastal and estuarine hydrodynamics with OPENCoastS," *Environ. Model. Softw.*, vol. 143, Sep. 2021, Art. no. 105132.

[45] D. Robinson, J. Cooper, and C. Gardner, "Modelling the relative permittivity of soils using soil hygroscopic water content," *J. Hydrol.*, vol. 255, nos. 1–4, pp. 39–49, 2002.

[46] J. R. Wang, "The dielectric properties of soil-water mixtures at microwave frequencies," *Radio. Sci.*, vol. 15, no. 5, pp. 977–985, Sep./Oct. 1980.

[47] *Electrical Characteristics of the Surface of the Earth*, ITU, Geneva, Switzerland, Tech. Rep., ITU-R P.527-4, 2017.

[48] E. Salahat, A. Kulaib, N. Ali, and R. Shubair, "Exploring symmetry in wireless propagation channels," in *Proc. Eur. Conf. Netw. Commun. (EuCNC)*, 2017, pp. 1–6.

[49] A. Fortunato, A. Oliveira, and A. M. Baptista, "On the effect of tidal flats on the hydrodynamics of the Tagus estuary," *Oceanologica Acta*, vol. 22, no. 1, pp. 31–44, 1999.

[50] J. M. Dias, J. M. Valentim, and M. C. Sousa, "A numerical study of local variations in tidal regime of Tagus estuary, Portugal," *PLoS ONE*, vol. 8, no. 12, pp. 1–15, 2013.

[51] Y. H. Lee, F. Dong, and Y. S. Meng, "Near sea-surface mobile radiowave propagation at 5 GHz: Measurements and modeling," *Radioengineering*, vol. 23, no. 3, pp. 824–830, Sep. 2014.

[52] E. Dinc and O. B. Akan, "Channel model for the surface ducts: Large-scale path-loss, delay spread, and AOA," *IEEE Trans. Antennas Propag.*, vol. 63, no. 6, pp. 2728–2738, Jun. 2015.

[53] W. Huang *et al.*, "Tidal simulation revisited," *Ocean Dyn.*, vol. 72, no. 3, pp. 187–205, 2022.

[54] M. Rodrigues, A. Rosa, A. Cravo, J. Jacob, and A. B. Fortunato, "Effects of climate change and anthropogenic pressures in the water quality of a coastal lagoon (Ria Formosa, Portugal)," *Sci. Total Environ.*, vol. 780, Aug. 2021, Art. no. 146311.

[55] A. Oliveira *et al.*, "OPENCoastS: An open-access service for the automatic generation of coastal forecast systems," *Environ. Model. Softw.*, vol. 124, Feb. 2020, Art. no. 104585.

Miguel Gutiérrez Gaitán (Member, IEEE) received the B.Sc. degree in electronics engineering from the Pontifical Catholic University of Valparaiso (PUCV), Valparaiso, Chile, in 2007, and the M.Sc. degree in telecommunications engineering from the Polytechnic University of Turin (PoliTo), Turin, Italy, in 2009. He is currently pursuing the Ph.D. degree in electrical and computer engineering with the Faculty of Engineering, University of Porto (FEUP), Porto, Portugal, under the supervision of Prof. Luís Almeida.

He is also an Assistant Professor with the Faculty of Engineering, Andrés Bello University (UNAB), Santiago, Chile, and a Research Fellow with the CISTER Research Center, Porto, where he collaborates in various national and international research projects, mainly in the areas of wireless networks, real-time communication, and the Internet of Things.

Pedro M. d'Orey received the Licenciatura degree in electrical and computer engineering from the University of Porto, Porto, Portugal, in 2004, the M.Sc. degree in telecommunications from the Queen Mary University of London, London, U.K., in 2008, and the Ph.D. degree in telecommunications from the University of Porto in 2014.

He was a Research Scientist with NEC Laboratories Europe, Heidelberg, Germany, and a Research and Development Engineer in the area of Mobile Communications. He is currently a Research Scientist with the CISTER Research Center, Porto, and an Invited Assistant Professor with the Faculty of Sciences, University of Porto. He has been involved in several European and international projects, in the Carnegie Mellon University (CMU) Portugal Program. His current research interests include wireless communications, automated vehicles, and AI/ML.

Dr. d'Orey received the Best Paper Award for four of his articles, namely at IEEE Vehicular Technology Conference (VTC) Spring and IEEE Vehicular Networking Conference (VNC) 2014.

José Cecílio received the Ph.D. degree in computer engineering from the University of Coimbra, Coimbra, Portugal, in 2013.

He is currently an Assistant Professor with the Faculty of Sciences, University of Lisbon, Lisbon, Portugal, and a Researcher with the Large Scale Computer Systems Laboratory (LASIGE). He is involved in several research projects in remote monitoring, the Internet of Things (IoT), adaptive and safety-critical cyber-physical systems (CPS), and reliable and energy-efficient systems. His research interests include wireless sensor networks, the IoT, embedded systems, distributed systems, and communication networks.

Marta Rodrigues received the B.Sc. degree in environmental engineering from the Instituto Superior Técnico, University of Lisbon, Lisbon, Portugal, in 2003, and the Ph.D. degree in biology from the University of Aveiro, Aveiro, Portugal, in 2012.

She was a Specialist in Ecology, Biodiversity, and Ecosystems Management. She is a Research Officer with the Laboratório Nacional de Engenharia Civil (LNEC), Lisbon, Portugal, with 15 years of experience in water quality modeling and monitoring. She joined the Estuaries and Coastal Zones Division of Hydraulics and Environment Department in 2005. Since 2005, she has been collaborating on several research and innovation projects, many related to water quality forecast systems and reliable monitoring.

Pedro M. Santos received the B.Sc. and M.Sc. degrees in electrical and computer engineering from the University of Porto, Porto, Portugal, in 2009, and the Ph.D. degree in electrical and computer engineering from the University of Porto in 2017.

He currently holds positions as a Research Scientist with the CISTER Research Center, Porto, and an Invited Lecturer with the University of Porto. He is also a PI of international projects, such as Eureka Information Technology for European Advancement (ITEA) Machine Intelligence for smart and sustainable planning and operation of IoT and Edge (MIRAI) and CMU-Portugal 5G/SDN Intelligent Systems For LOw latencY V2X communications in cross-Domain mobility applications (FLOYD), and Portuguese, such as NORTE 2020 REal-Time support Infrastructure and Energy management for Intelligent carbon-Neutral smArt cities (RETINA). He has been participating as a Researcher in numerous projects, such as P2020, CMU-Portugal, Framework Programme 7 (FP7), and Horizon 2020 (H2020) Electronic Components and Systems for European Leadership (ECSEL). His research interests include wireless propagation, networking, the Internet of Things, and edge computing.

Dr. Santos serves regularly as a TPC Member for IEEE Vehicular Networking Conference (VNC), International Conference on Factory Communication Systems (WCFS), and European Alliance for Innovation (EAI) Future5V, and is a Reviewer for several forums on communications and networking, such as IEEE Transactions on Wireless Communications (IEEE TWC), VNC, and IEEE Vehicular Technology Conference (VTC).

Luís Pinto received the M.Sc. degree in electrical and computer engineering from the Faculty of Engineering, University of Porto (FEUP), Porto, Portugal, in 2011, and the Ph.D. degree in drone communications and networks from Carnegie Mellon University, Pittsburgh, PA, USA, in 2018.

He is currently an invited Assistant Professor with the Department of Informatics, University of Lisbon, Lisbon, Portugal. His research interests include wireless networks, embedded systems, and robotics.

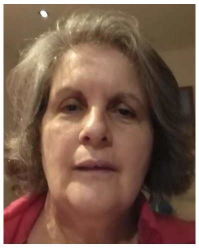

Anabela Oliveira received the B.Sc. degree in civil engineering from the University of Lisbon, Lisbon, Portugal, in 1990, and the Ph.D. degree in environmental science and engineering from Oregon Health and Science University, Portland, OR, USA, in 1997.

In 1990, she joined the National Laboratory for Civil Engineering (LNEC), Lisbon, Portugal, where she is a Senior Researcher and the Head of the Information Technology in Water and Environment Division, Hydraulics and Environment Department. Her research focuses on forecast systems, environmental modeling, and surveillance.

António Casimiro (Member, IEEE) received the Ph.D. degree in informatics from the University of Lisbon, Lisbon, Portugal, in 2003.

In 1996, he joined the Department of Informatics, Faculty of Sciences (FCUL), University of Lisbon, where he is an Associate Professor and a member of the LASIGE Research Laboratory, leading the research line on cyber-physical systems. His research focuses on architectures, fault tolerance, and adaptation in distributed and real-time embedded systems, with applications on cyber-physical systems like autonomous and cooperative vehicles or monitoring and control systems in critical infrastructures.

Dr. Casimiro is a member of the International Federation for Information Processing (IFIP) WG10.4 on Dependable Computing and Fault Tolerance, the Ada-Europe Board, European Workshop on Industrial Computer Systems (EWICS) TC7, Association for Computing Machinery (ACM), and the Ordem dos Engenheiros.

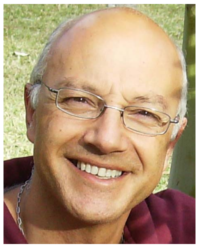

Luís Almeida (Senior Member, IEEE) received the Ph.D. degree in electrical engineering from the University of Aveiro, Aveiro, Portugal, in 1999.

He is currently an Associate Professor with the Electrical and Computer Engineering Department, University of Porto, Porto, Portugal, where he coordinates the Distributed and Real-Time Embedded Systems Laboratory (DaRTES). He is also the Vice-Director of the CISTER Research Center on Real-Time and Embedded Computing Systems, Porto. He participated in numerous funded national and international research projects and regularly participates in the organization of scientific events in real-time communications for distributed industrial/embedded systems, for teams of cooperating agents and sensor networks.

Mr. Almeida was the Chair of the IEEE Technical Committee on Real-Time Systems (TCRTS) from 2020 to 2021 and is the Chair of the EDAA Special Interest Group on Embedded Systems (EMSIG). He was the Program Chair and the General Chair of the IEEE Real-Time Systems Symposium in 2011 and 2012, respectively, the Local Co-Chair in 2016, and the General Co-Chair of CPSweek in 2018. He is the Editor-in-Chief of the *Real-Time Systems* (Springer), and an Associate Editor of the *Journal of Systems Architecture* (Elsevier) and the *International Journal of Advanced Robotic Systems* (SAGE). He was also a Trustee of the RoboCup Federation from 2008 to 2016 and the Vice-President from 2011 to 2013.